

## Nylon Electrolyte Chemistry in High-energy Li-metal Batteries

Zhiming Zhao,<sup>\*ab</sup> Georgian Melinte,<sup>c</sup> Dong Guo,<sup>ab</sup> Yongjiu Lei,<sup>ab</sup> Mohamed N. Hedhili,<sup>c</sup> Xianrong Guo,<sup>c</sup>  
Zixiong Shi,<sup>ab</sup> Yizhou Wang,<sup>ab</sup> Jehad K. El-Demellawi,<sup>d</sup> Wenli Zhao,<sup>ab</sup> Husam N. Alshareef<sup>\*ab</sup>

<sup>a</sup>Center for Renewable Energy and Storage Technologies (CREST), King Abdullah University of Science and Technology (KAUST), Thuwal 239955-6900, Saudi Arabia. E-mail: [zhiming.zhao@utexas.edu](mailto:zhiming.zhao@utexas.edu) (Z. Zhao); [husam.alshareef@kaust.edu.sa](mailto:husam.alshareef@kaust.edu.sa) (H. N. Alshareef)

<sup>b</sup>Materials Science and Engineering, Physical Science and Engineering (PSE) Division, King Abdullah University of Science and Technology (KAUST), Thuwal 239955-6900, Saudi Arabia.

<sup>c</sup>Core Labs, King Abdullah University of Science and Technology (KAUST), Thuwal 23955-6900, Saudi Arabia.

<sup>d</sup>KAUST Upstream Research Center (KURC), EXPEC-ARC, Saudi Aramco, Thuwal 23955-6900, Saudi Arabia.

# 1. Methods

## Materials

EC (>99%), DEC (>99%), and FEC (>99%) were procured from Fisher US and dehydrated using 4 Å molecular sieves prior to use. Lithium hexafluorophosphate (LiPF<sub>6</sub>, battery grade, ≥99.99% trace metals basis) was purchased from Sigma Chemicals. PA 6 non-woven fabrics (M<sub>w</sub> = 40,000) were obtained from XUANYUHONG Technology, Beijing, and dried at 80 °C overnight under vacuum. LiPF<sub>6</sub> and PA6 were dissolved in a mixture of solvents (EC: DEC= 1:1, vol%, with 5 wt.% FEC) at predetermined concentrations within an argon-filled glovebox (water < 0.1 ppm, O<sub>2</sub> < 0.1 ppm). The NCM811 single-crystal cathode (SY3204), coated on aluminum foil with a mass loading of 21.5 mg cm<sup>-2</sup> (active mass ratio 94.5%), was purchased from Canrd New Energy Technology Co., Ltd., Guangdong, China. The glass fiber separator, with a thickness of 0.4 mm, was purchased from Whatman.

## Assembly of cells and electrochemical measurements

CR2032 coin-type cells were assembled using various electrolytes and electrodes. To maintain consistency across experiments, each coin cell was infused with a fixed volume of 40 μL of electrolyte. For the cells incorporating PAE, the PAE was heated to 60 °C to enhance its liquidity, enabling it to be easily drawn up by a pipette. The cycling tests for all Li||NCM811 cells commenced with two formation cycles at a charge and discharge rate of 0.1 C, where 1 C corresponds to 200 mA g<sup>-1</sup>. During the charging phase, a constant voltage of 4.4 V was applied until the current fell below 0.02 C or the duration of the constant-voltage charging exceeded 20 minutes. For the 50 μm Li||NCM811 cells, the N/P ratio was calculated as 2.5. Electrochemical impedance spectroscopy (EIS) measurements were conducted across a frequency range from 10 Hz to 1 MHz at various temperatures.

A pouch cell was constructed utilizing an NCM811 cathode, lithium metal, and a specially prepared electrolyte. The dimensions of the cathode and anode are 90 mm × 100 mm and 95 mm × 105 mm, respectively. The lithium metal anode, approximately 50 μm thick, was compressed onto a copper mesh prior to assembly. The assembly process involved stacking the cathode, separator, and the lithium anode foil sequentially, with the entire assembly subsequently encapsulated within an aluminum plastic film package. For the pouch cells, the NCM811 loading on the cathode was approximately 3.66 g across two layers. The mass of the lithium foil used was

about 0.53 mg for two layers, and the electrolyte mass totaled 2.923 g. Assembly of the pouch cells was conducted in a dry room, where the dew point was meticulously controlled at around  $-60\text{ }^{\circ}\text{C}$ . For the calculation of energy density, the capacity and average discharge voltage from the 10th cycle were utilized. The capacity recorded on the 10th cycle was 692.12 mAh, and the average discharge voltage was 3.787 V. Considering the combined mass of the active materials in the cathode, anode, and electrolyte, totaling 6.595 g, the energy density was calculated to be approximately  $397\text{ Wh kg}^{-1}$ . The testing of the coin cells and pouch cells was conducted under  $20\text{ }^{\circ}\text{C}$ .

## Characterizations

All the cycled electrodes were extracted from the corresponding cells after 50 cycles and washed with dimethyl carbonate (DMC) solvent, followed by XPS, ToF-SIMS, and TEM characterizations. To avoid exposure to air and moisture, samples were transferred directly to the XPS vacuum holder inside a glovebox. High-resolution XPS spectra were obtained using a Kratos Axis Ultra DLD spectrometer equipped with a monochromatic Al K $\alpha$  X-ray source ( $h\nu = 1486.6\text{ eV}$ ) operating at 75 W. This system includes a multichannel plate, an Ar $^{+}$  etching gun, and a delay line detector under a vacuum of  $1\sim 10^{-9}$  mbar. Samples were mounted in floating mode to minimize differential charging, with charge neutralization applied to all samples. Binding energies were calibrated to the sp $^2$ /sp $^3$  hybridized carbon of the C 1s peak at 284.6 eV. ToF-SIMS analyses were performed using a PHI nanoTOF II system. A Cs gun served as the sputtering source with 1 keV energy in negative ion mode. The sputtering and collection areas were  $330 \times 330\text{ }\mu\text{m}^2$  and  $80 \times 80\text{ }\mu\text{m}^2$ , respectively.

Raman spectra were obtained with a WITec Apyron Alpha 300, where electrolytes sealed in NMR thin-wall tubes were subjected to a Raman laser with a wavelength of 532 nm and power of 60 mW. The system configuration included a Raman CCD1 with a G2:1800 g mm $^{-1}$  grating at BLZ = 500 nm, and the accumulation time was set to 2000. NMR spectra were recorded at  $60\text{ }^{\circ}\text{C}$  using a Bruker 600 MHz AVANCE III NMR spectrometer with a BBFO probe. The tests conducted at elevated temperatures are designed to ensure that the PAE remains in a liquid state. Double-wall NMR tubes minimized interference from deuterium reagents and reference chemicals. The inner tube contained 0.02 M LiPF $_6$  in deuterated-DMSO, and the outer tube held the sample. The  $^1\text{H}$ - $^{19}\text{F}$  HOESY experiment employed a non-gradient QNP operation, with a  $^{19}\text{F}$  90-degree pulse ranging from 14-17  $\mu\text{s}$ , a  $^1\text{H}$  90-degree pulse of 11  $\mu\text{s}$ , mixing times from 0.6-2.5s, and 112-160 scans. The

morphology of the samples was characterized by a scanning electron microscope (SEM, Teneo). The AFM images were obtained on Dimension Icon Atomic Force Microscope system (Bruker, Santa Barbara, CA). DSC measurements were tested from room temperature to 260 °C and then to -90 °C at 5 °C min<sup>-1</sup> (DSC-TA Discovery 250). Samples were first heated to 260 °C and maintained for 5 min to eliminate thermal history. Polarized light microscopy were done using polarizing microscope (Olympus-BX51, Japan). Storage modulus, loss modulus, and viscosity measurement of PAE were done using a parallel-plate rheometer (ARES-G2, TA Instrument) at 25 °C. The diameter of the parallel plate is 8 mm and the thickness was set as 0.6 mm. Frequency sweep was performed at 0.05% strain at a fixed temperature (25°C).

For preparing cryo-TEM samples, Li||Cu cells were assembled using a 300-mesh Cu TEM grid with lacey carbon films as the current collector. The cells underwent discharge at a current density of 1 mA cm<sup>-2</sup> for 6 minutes (areal density: 0.1 mAh cm<sup>-2</sup>). Subsequently, the cells were disassembled in an argon-filled glovebox to extract the TEM grid. This grid was thoroughly cleaned with DMC, dried, and then securely sealed within a small polypropylene tube inside the glovebox. The sealed tube was transferred to a cryo-transfer station filled with liquid nitrogen, where it was crushed to expose the grid directly to liquid nitrogen. The prepared grids were loaded onto a Gatan cryo-TEM holder in the cryo-transfer station. The holder was kept at liquid nitrogen temperature for cryo-TEM imaging, utilizing a dewar tank filled with liquid nitrogen mounted directly onto the holder. The low-dose bright-field TEM images were obtained on a Titan 300 transmission electron microscope (ThermoFisher™) operating at 300 kV. The low-dose TEM images were recorded on a OneView Gatan™ camera, with the acquisition parameters (exposure, frame size or rate) adjusted based on the imaging conditions (sample stability, mechanical drift, etc.). The cathode samples were measured on a ThemisZ (ThermoFisher™) operated at 300kV acceleration voltage. The CEI layers were analyzed at room temperature conditions in the TEM mode using a Ceta camera. For the STEM-HAADF imaging, FIB lamellas were prepared for each sample using a Helios G4 (ThermoFisher™) dual-beam microscope. Low milling currents and low ion-beam voltages of 5kV and 2kV were used for obtaining thin and amorphous-free TEM lamellas. The HAADF inners angle was set to 47 mrad while the probe converge angle was 21 mrad.













### **Computational details**

In the molecular dynamic simulations, all ions and molecules were modeled using the all-atom

optimized potentials for liquid simulations (OPLS-AA) force field.<sup>1</sup> The molecular force field parameters were sourced from the LigParGen web server,<sup>2</sup> and the charges were scaled to 1.14\*CM1A.<sup>3</sup> To enhance simulation accuracy, ion charges were adjusted using a 0.8 scaling factor. All structural optimizations were conducted using ORCA 5.0.4 software at the B97-3c level, followed by single-point energy and wavefunction calculations at the B3LYP/G D3 def2-TZVP def2/J RIJCOSX level. Initial atomic coordinates were generated using the Packmol program, optimizing molecular packing within a  $60 \times 60 \times 60 \text{ \AA}^3$  periodic box to create a bulk system (Table S6-S7).

The MD simulations were carried out with GROMACS 2019.5, employing a combination of the steepest descent method (5000 steps) and the conjugate gradient method (5000 steps) for system optimization.<sup>4</sup> Subsequent equilibration was achieved using a time constant of 1 fs within a canonical ensemble, employing V-rescale temperature coupling and the Parrinello-Rahman barostat to maintain stable conditions at 298 K and 1 atm. Post-equilibrium, the Berendsen method was applied, with the LINCS algorithm constraining bond lengths and angles. Van der Waals forces were considered, and long-distance electrostatic interactions were managed via the Particle-Mesh Ewald method. Trajectory data were saved every 10 ps to document the simulation progress.

## 2. Supplementary data and tables

DEC	 ~2 min	 ~5 min		
DME	 ~3 min	 ~10 min		
H <sub>2</sub> O				
	1M LiPF <sub>6</sub>	1M LiFSI	1M NaPF <sub>6</sub>	1M KPF <sub>6</sub>

**Fig. S1** The dissolution ability of PA 6 in various solutions—carbonate (DEC), ether (dimethoxyethane, DME), and aqueous—with different salts. The concentrations of salt and PA 6 are 1M and 2 wt.%, respectively. The times displayed in the insets of the Fig.s indicate the dissolution time when heated at 60 °C.

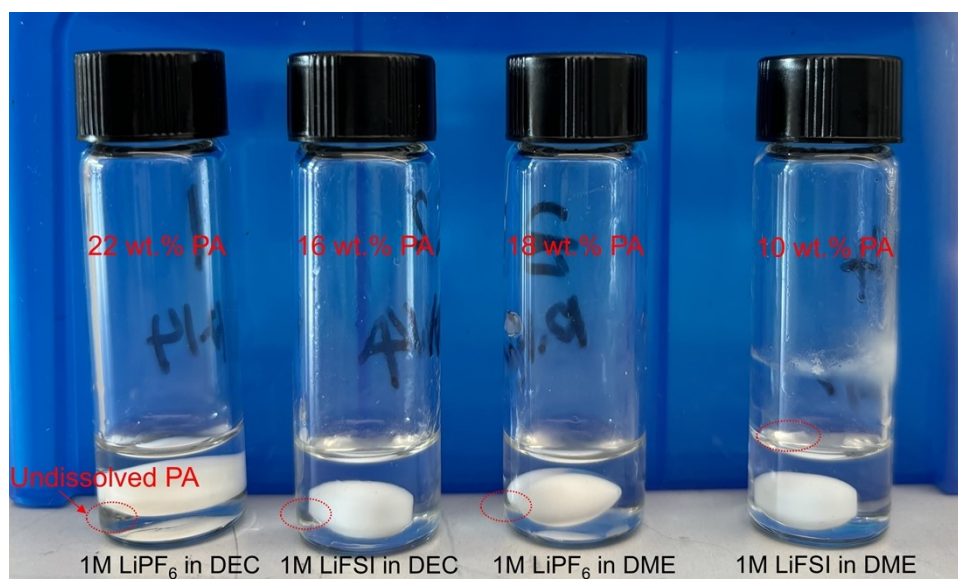


**Fig. S2** Determination of maximum concentrations of PA in various solutions. This Fig. illustrates the maximum solubility of PA in different electrolyte solutions: 1M LiPF<sub>6</sub> in DEC, 1M LiFSI in DEC, 1M LiPF<sub>6</sub> in DME, and 1M LiFSI in DME. For each solution, PA was added incrementally in 2 wt.% increments until undissolved PA was observed after stirring 2 hours at 60 °C, indicated by red circles. This process establishes the solubility limit of PA in each solvent.



**Fig. S3** The dissolution status of 2 wt.% PA 6 and PA 12 in 1M LiPF<sub>6</sub> in DEC.



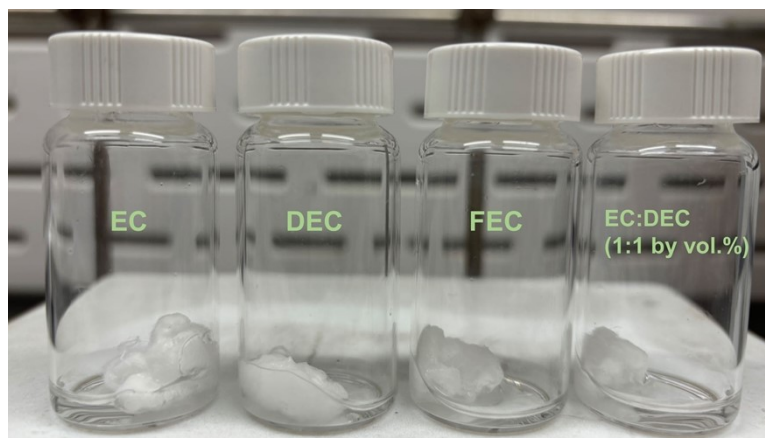


**Fig. S4** The dissolution status of PA in different carbonate solvents at 60°C (PA concentration: 2 wt.%).

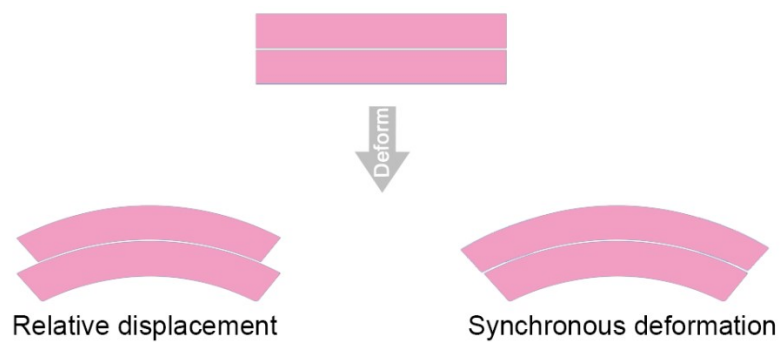


**Fig. S5** Illustration of relative displacement and synchronous deformation of battery components in layered batteries. This Fig. highlights the necessity of high viscosity of electrolytes to achieve synchronous deformation within the battery structure.

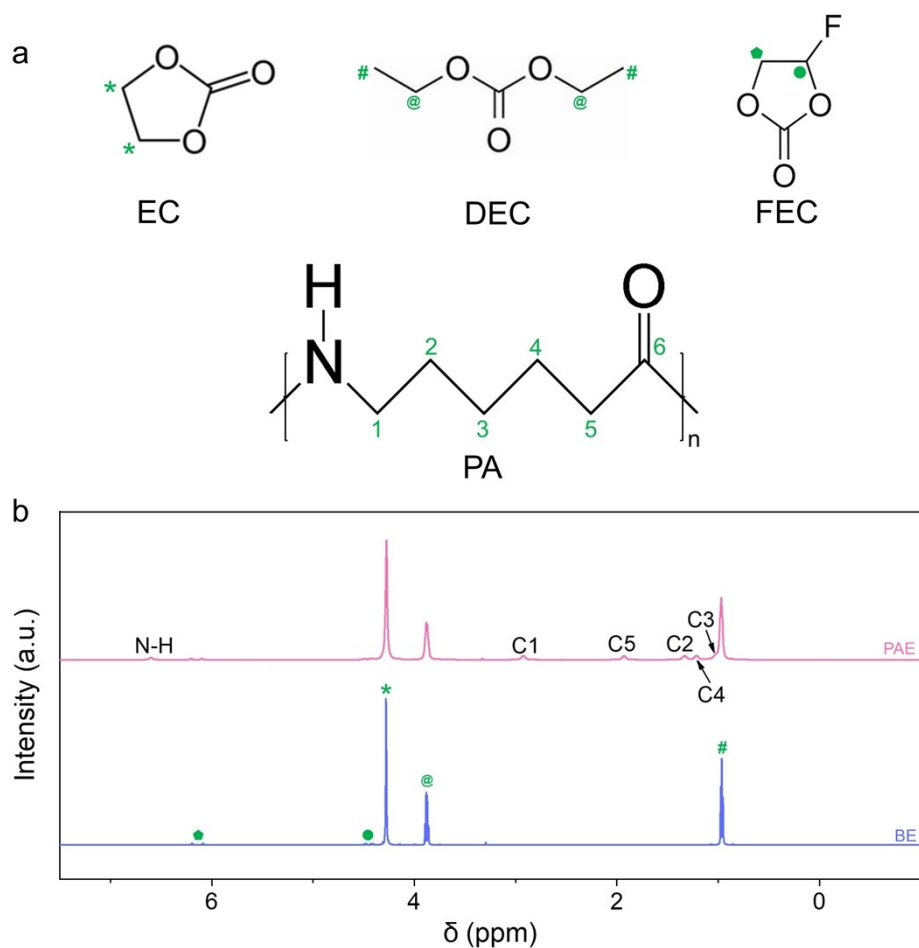


**Fig. S6** (a) Molecular structure of carbonate molecules and the PA 6 polymer, with H-nuclei positions indicated by distinct symbols. (b)  $^1\text{H}$  NMR spectra of BE and PAE, with peaks corresponding to the H-nuclei marked in (a).

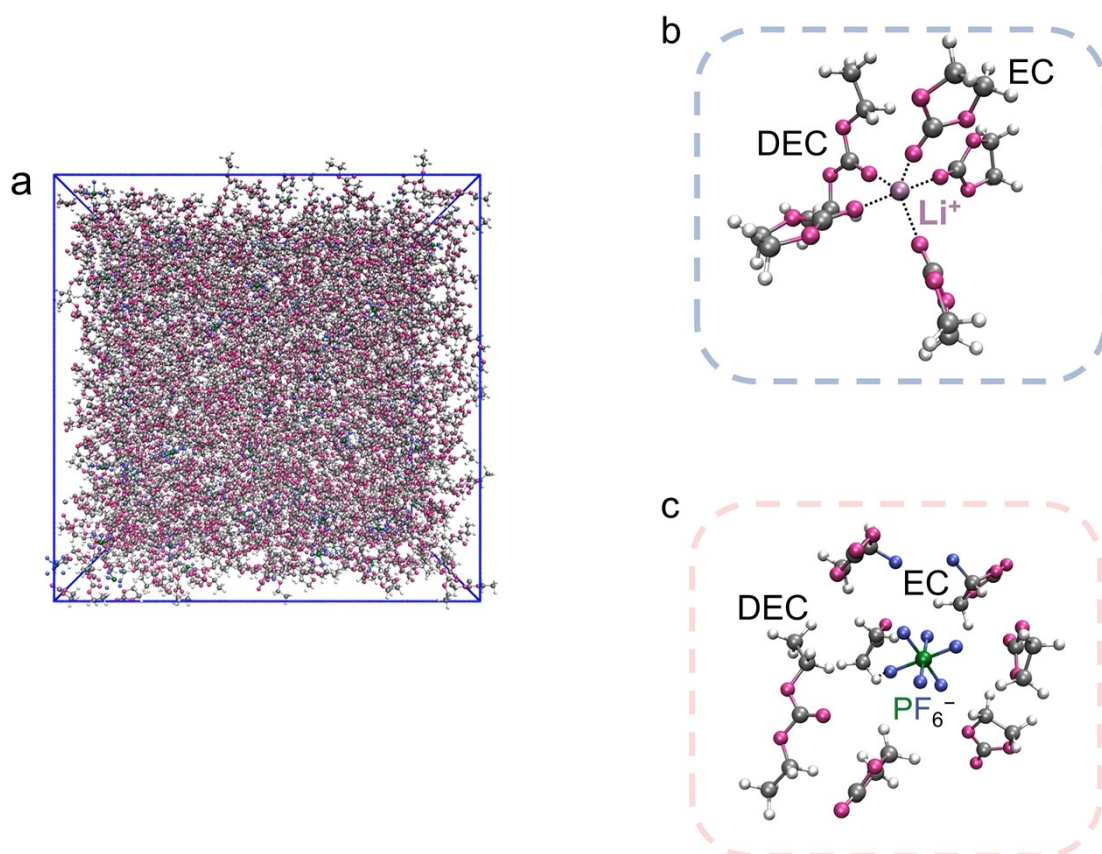


**Fig. S7** (a) Equilibrium molecular dynamics (MD) simulation snapshots for BE. (b) Typical  $\text{Li}^+$  chemical environment in BE. (c) Typical  $\text{PF}_6^-$  chemical environment in BE.

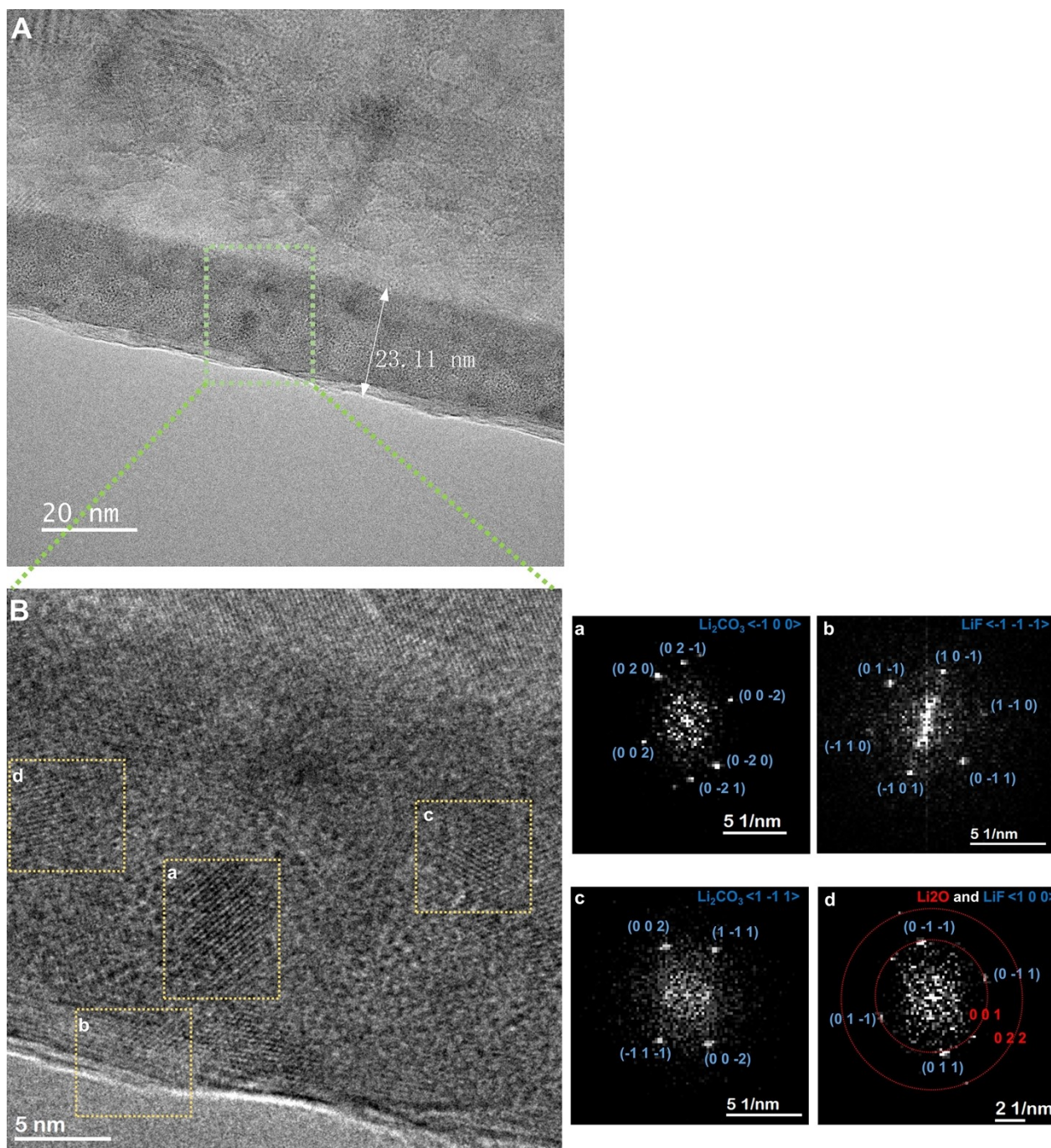


**Fig. S8** (A) Cryo-TEM image depicting the boundary of a lithium deposit in BE on a copper mesh TEM grid, highlighting segments of the SEI. (B) An enlarged Cryo-TEM image of the area within the light-green rectangle in (A). (a-d) Fast Fourier Transform (FFT) patterns obtained from various specific areas illustrated in (B). Please note that (B) is the same image with Fig. 5f but with different rotation. The lattice parameters used for the assignment of the diffraction spots are listed in Table S1-S4.



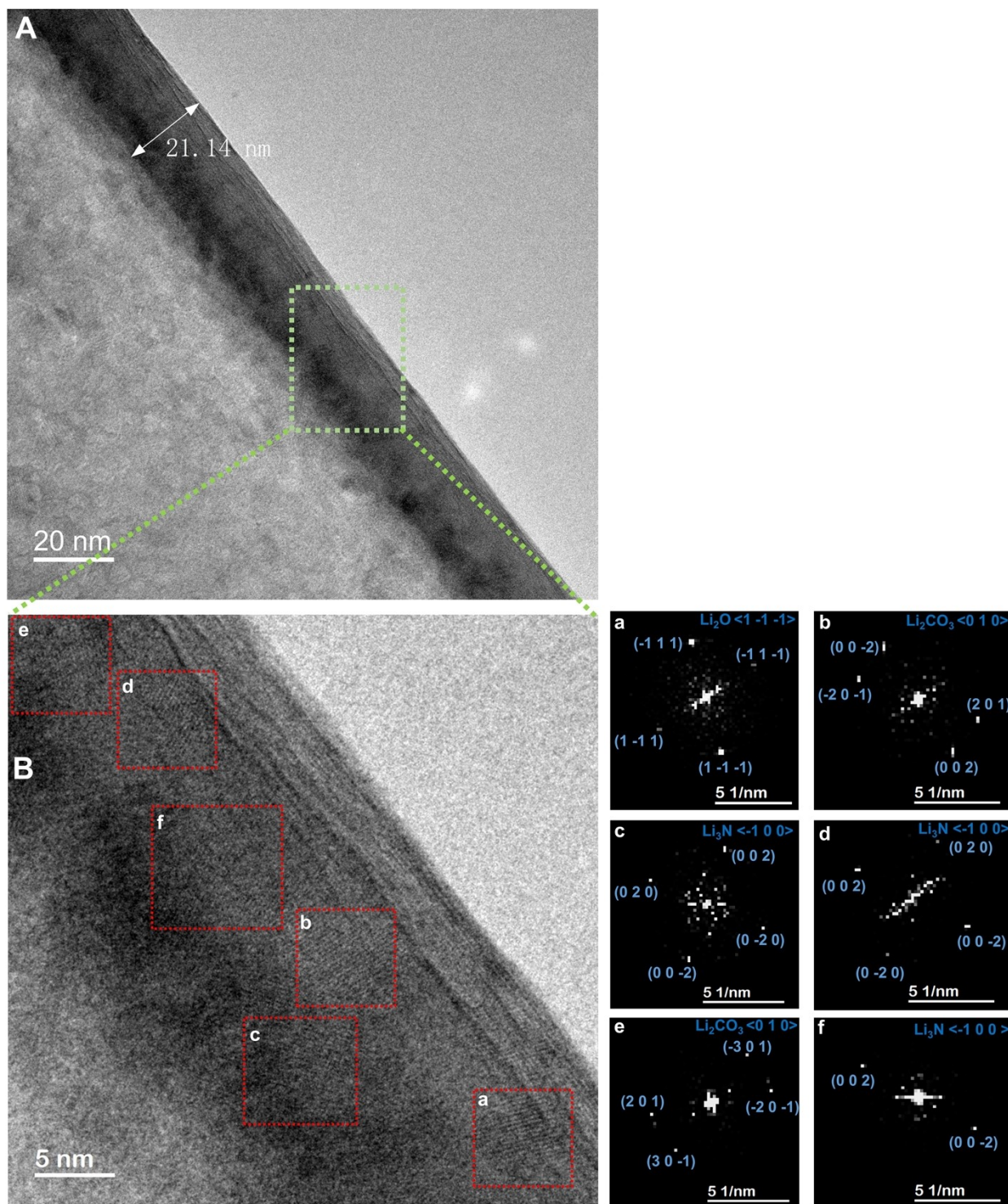


**Fig. S9** (A) Cryo-TEM image depicting the boundary of Li deposits in PAE on a copper mesh TEM grid, highlighting segments of the SEI. (B) An enlarged Cryo-TEM image of the area within the light-green rectangle in (A). (a-f) FFT patterns obtained from various specific areas illustrated in (B). Please note that (B) is the same image with Fig. 5g but with different rotation. The lattice parameters used for the assignment of the diffraction spots are listed in Table S1-S4.

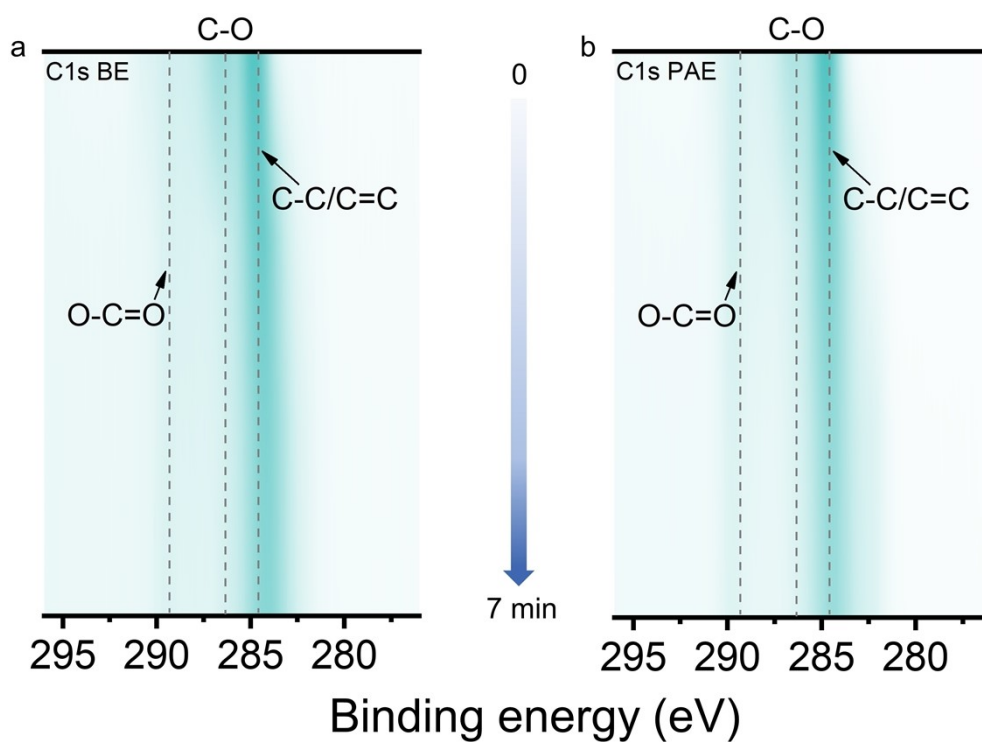


**Fig. S10** 2D C1s contour HR-XPS data of SEI on Li metal formed in: (a) BE, (b) PAE.

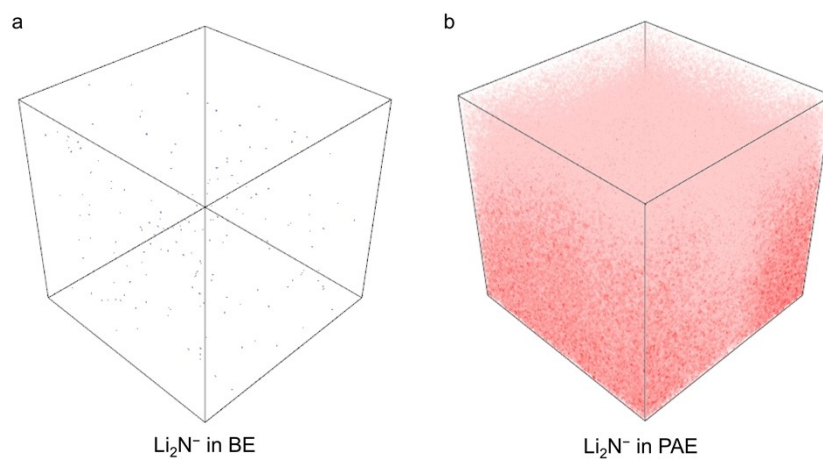


**Fig. S11** ToF-SIMS 3D reconstruction of  $\text{Li}_2\text{N}^-$  species on Li anodes after cycling in (a) BE and (b) PAE.



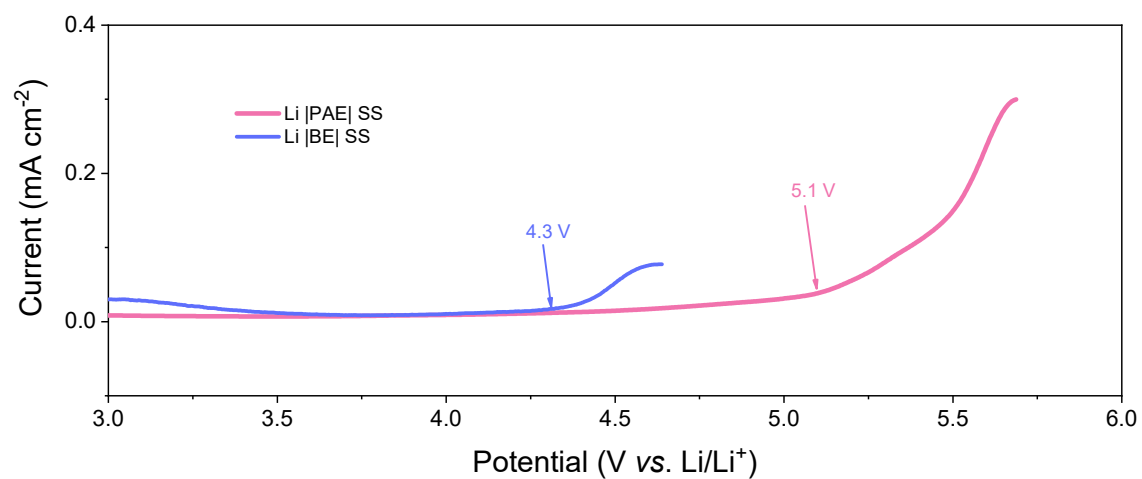


**Fig. S12** Linear sweep voltammetry (LSV) test of the Li||SS cell with different electrolytes (scanning rate: 1 mV s<sup>-1</sup>).

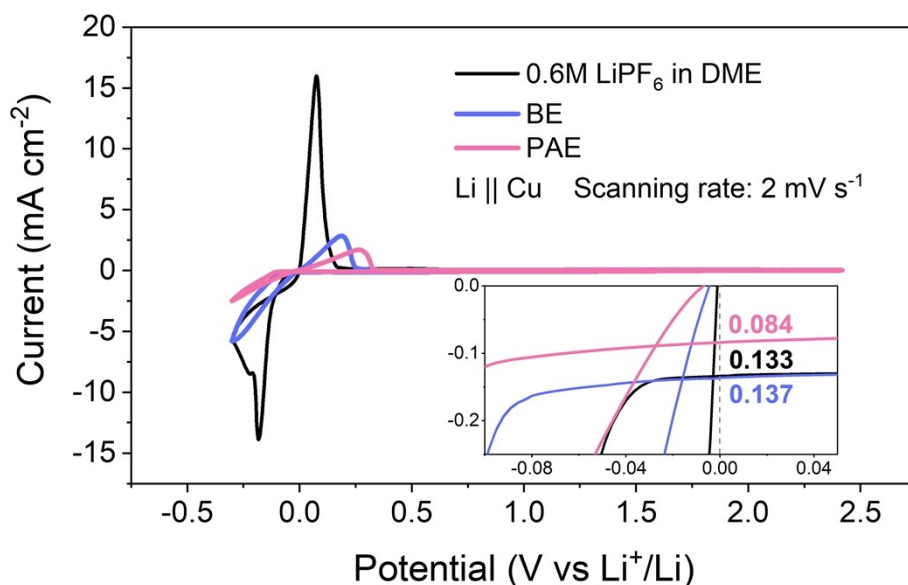


**Fig. S13** CV test of the Li||Cu cell with different electrolytes. The inset shows the enlarged current response curve near 0 V vs. Li<sup>+</sup>/Li, where the reduction decomposition current densities of different electrolytes are listed.

We tested the reduction stability of our Nylon electrolyte (PAE), a standard carbonate electrolyte (1 M LiPF<sub>6</sub> in EC: DEC (1:1 by vol%) + 5 wt.% FEC), and an ether electrolyte (0.6 M LiPF<sub>6</sub> in DME, which is the highest concentration of LiPF<sub>6</sub> that can be prepared at room temperature in our lab) using Li||Cu cells. As demonstrated in **Fig. S13**, near 0 V vs. Li<sup>+</sup>/Li, the reduction decomposition current of PAE is significantly lower than that of both the carbonate and ether electrolytes. This high reduction stability in PAE can be attributed to the reduced presence of small solvent molecules, the stabilization of anions, and a macromolecule-enriched solvation shell surrounding Li<sup>+</sup>. These factors collectively contribute to the superior performance of PAE under reduction conditions.

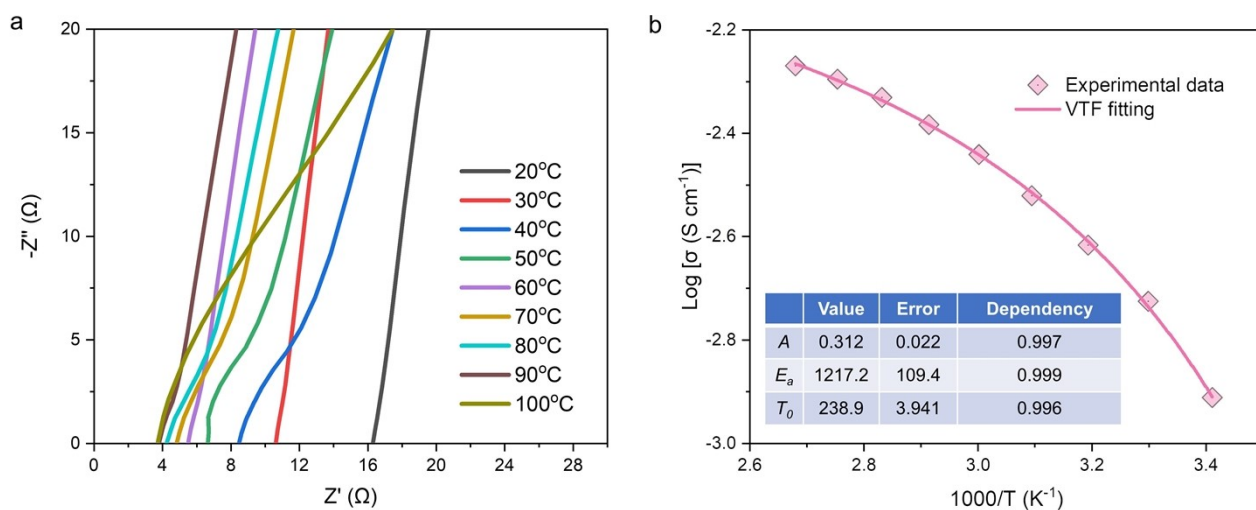


**Fig. S14** (a) Electrochemical impedance spectroscopies (EIS) of SS|PAE|SS (SS: stainless steel) cell at various temperatures from 20 to 100 °C. (b) Vogel–Tammann–Fulcher (VTF) plots of conductivity versus temperature for PAE.

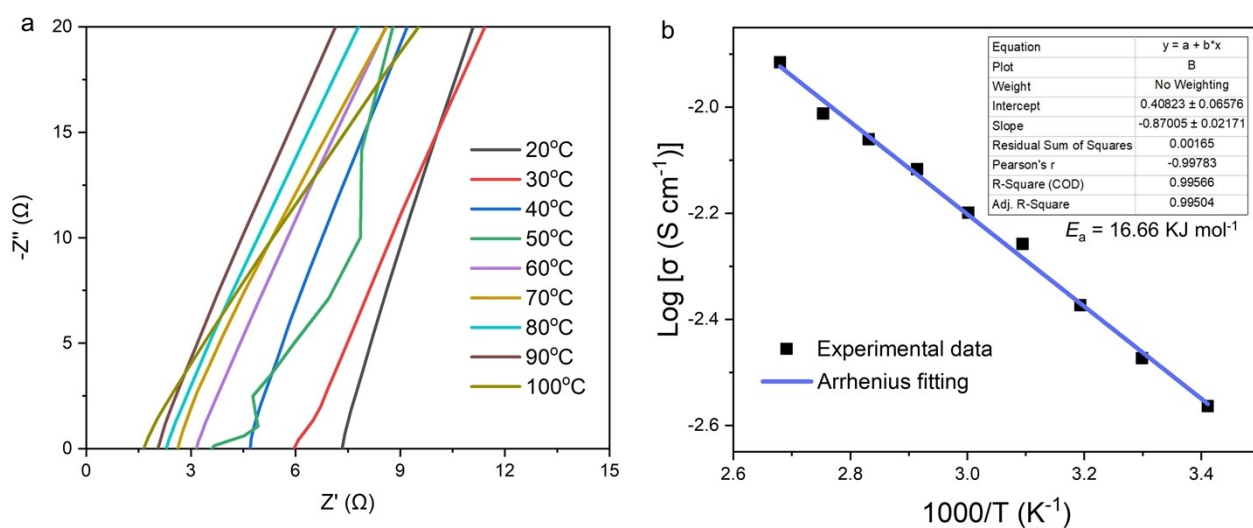


**Fig. S15** (a) EIS plots of SS|BE|SS cell at various temperatures from 20 to 100 °C. (b) Arrhenius fitting for ionic conductivity of BE at various temperatures.

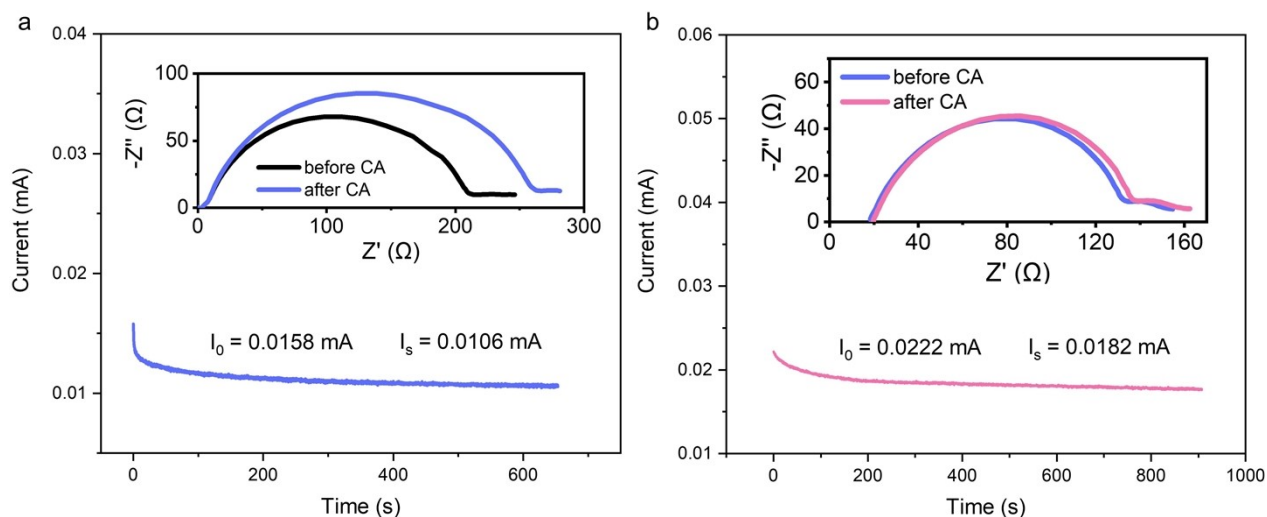


**Fig. S16** Test of  $\text{Li}^+$  transference number in (a) BE, and (b) PAE. DC polarization curve of the symmetrical  $\text{Li}||\text{Li}$  cell at  $20^\circ\text{C}$ . (Inset shows the AC complex impedance plot before and after DC polarization of symmetrical  $\text{Li}$  cell).

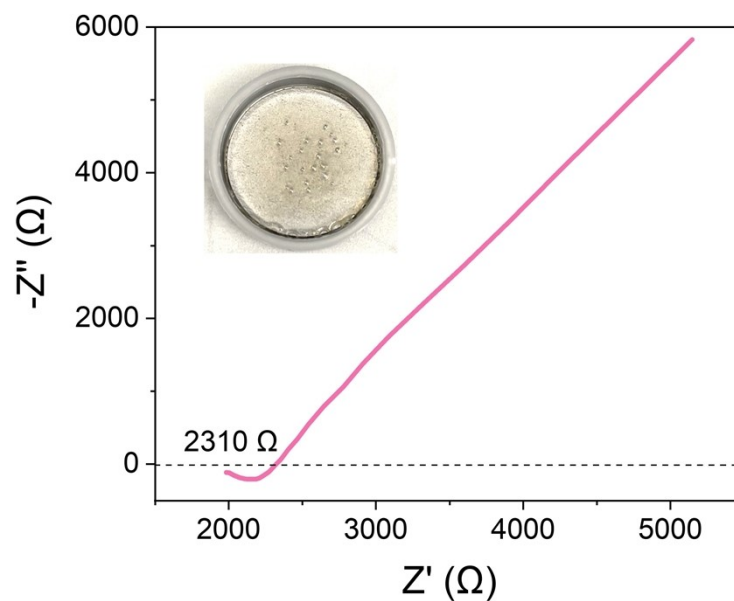


**Fig. S17** EIS plot of SS | solvent-free PAE | SS cell at 20°C. The inset shows the transparent PAE membrane. Preparation process of the solvent-free membrane: 80  $\mu\text{L}$  of PAE was dropped onto the SS in a 2032 battery case, then dried at 120°C under vacuum for 48 hours. It was subsequently transferred to a glovebox, where it was stored for 3 days before assembling the cell. The thickness of the membrane is measured to be  $\sim 100 \mu\text{m}$ .

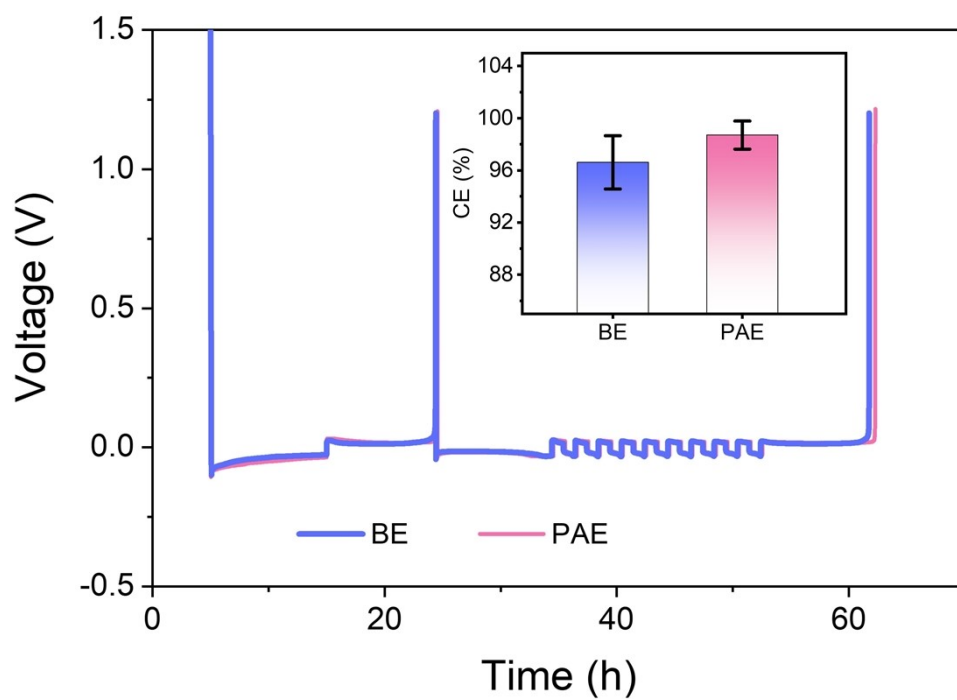


**Fig. S18** CE of Li||Cu cells with various electrolytes using the modified Aurbach's method at a current density of  $0.5 \text{ mA cm}^{-2}$  (Inset shows the average CE of three parallel cells with standard deviation).

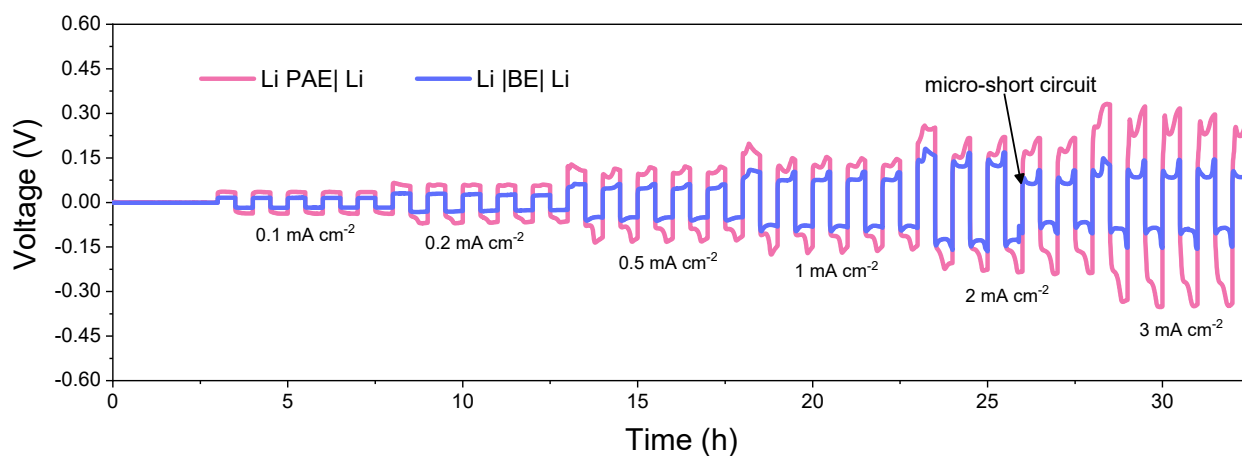


**Fig. S19** Rate performance of symmetrical Li cells using different electrolytes. The cell with BE underwent a micro-short circuit at  $2 \text{ mA cm}^{-2}$ .



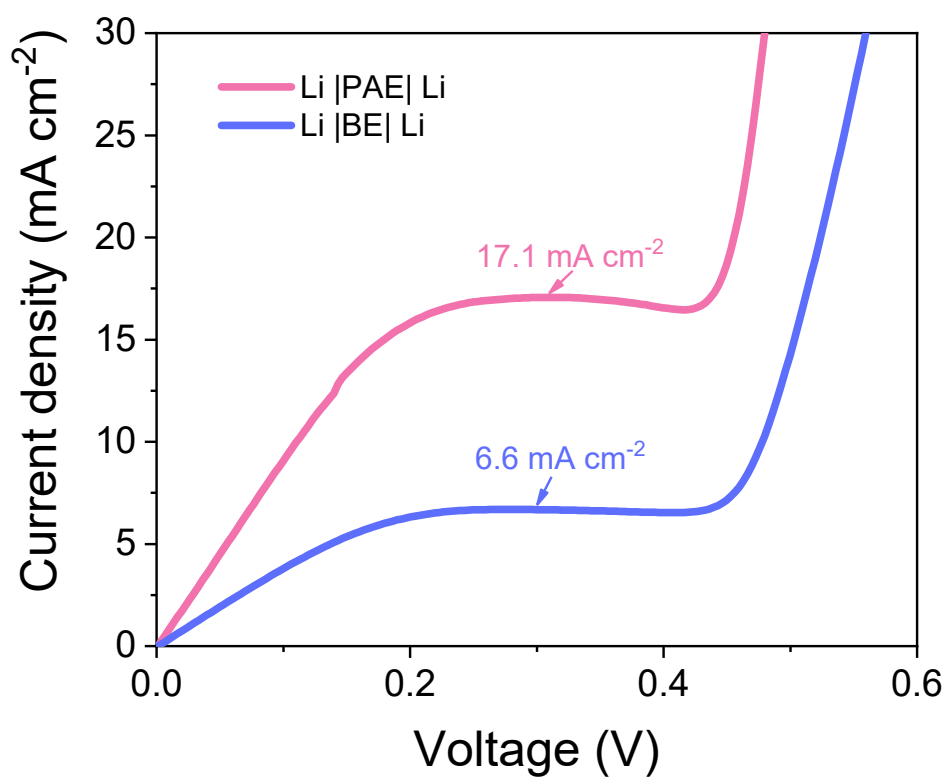


**Fig. S20** LSV test for measuring the limiting current in symmetrical Li cells with different electrolytes (scanning rate: 1 mV s<sup>-1</sup>). Before LSV test, the cells underwent 20 cycles at a current density of 0.5 mA cm<sup>-2</sup> (0.5 mAh cm<sup>-2</sup>) to facilitate the formation and stabilization of SEI on Li metal.

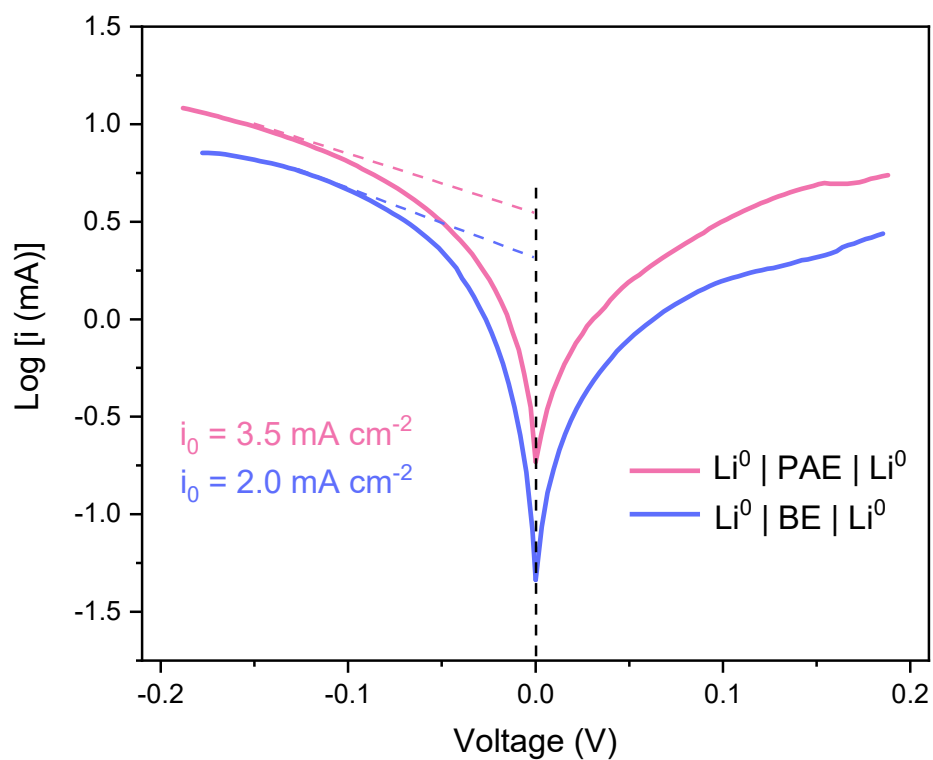


**Fig. S21** The Tafel plots of symmetric Li cells using various electrolytes after 20 galvanostatic cycles.

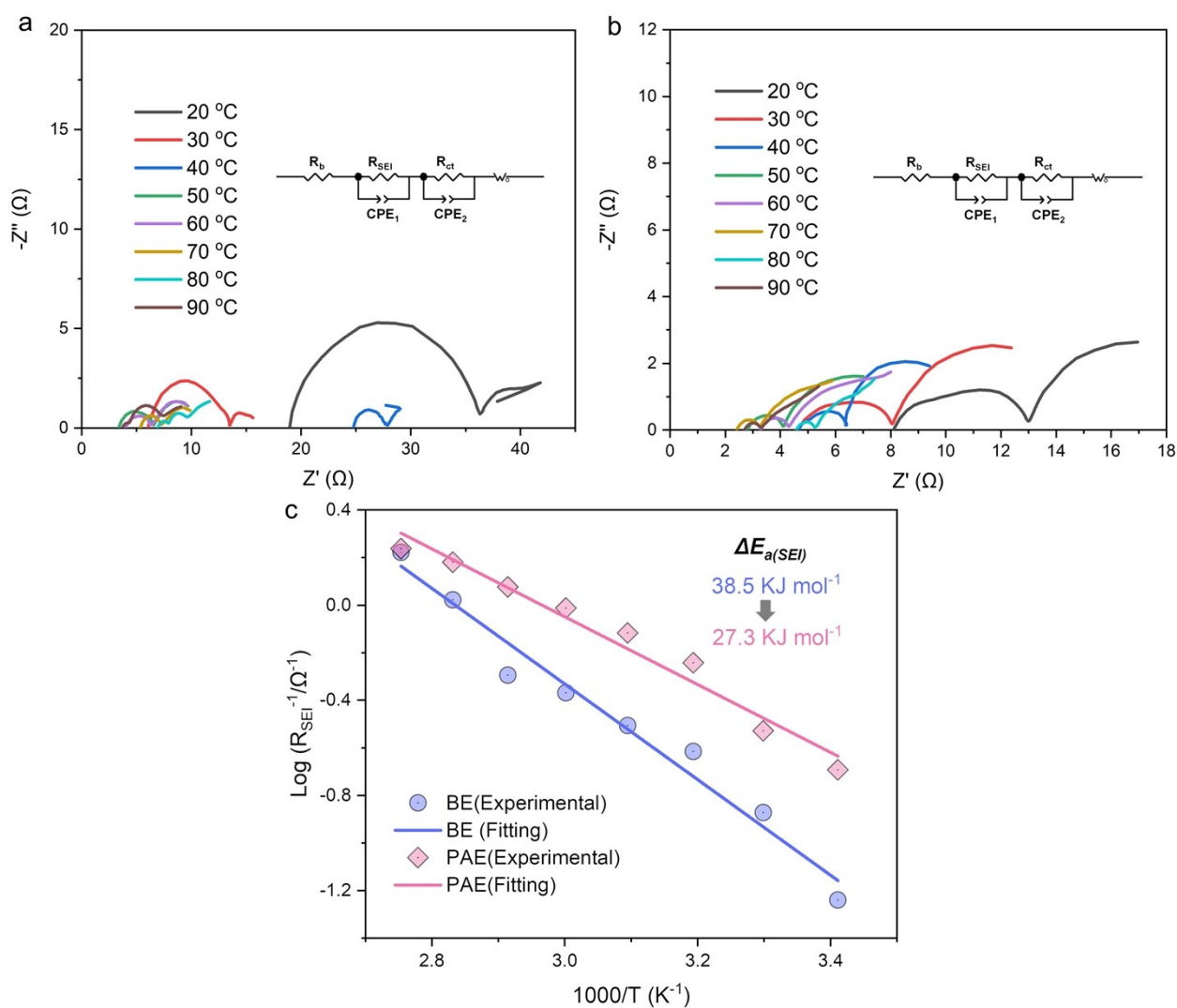


**Fig. S22** EIS of symmetrical Li cell with (a) BE and (b) PAE at different temperatures after forming stable SEI (under galvanostatic condition for 20 cycles,  $0.5 \text{ mA cm}^{-2}$  with a capacity of  $0.5 \text{ mAh cm}^{-2}$  for each half cycle). (c) Arrhenius behavior of the reciprocal resistances corresponding to interfacial components as a function of the reciprocal temperature.

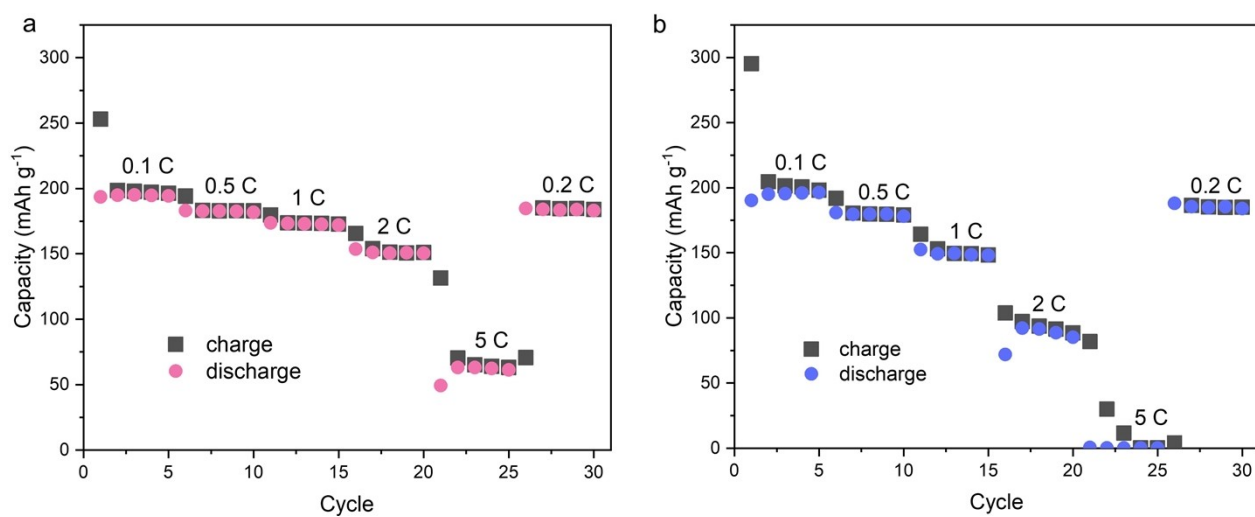


**Fig. S23** Rate performances of 50  $\mu\text{m}$  Li||NCM811(4.06 mAh cm<sup>-2</sup>) using (a) PAE and (b) BE.

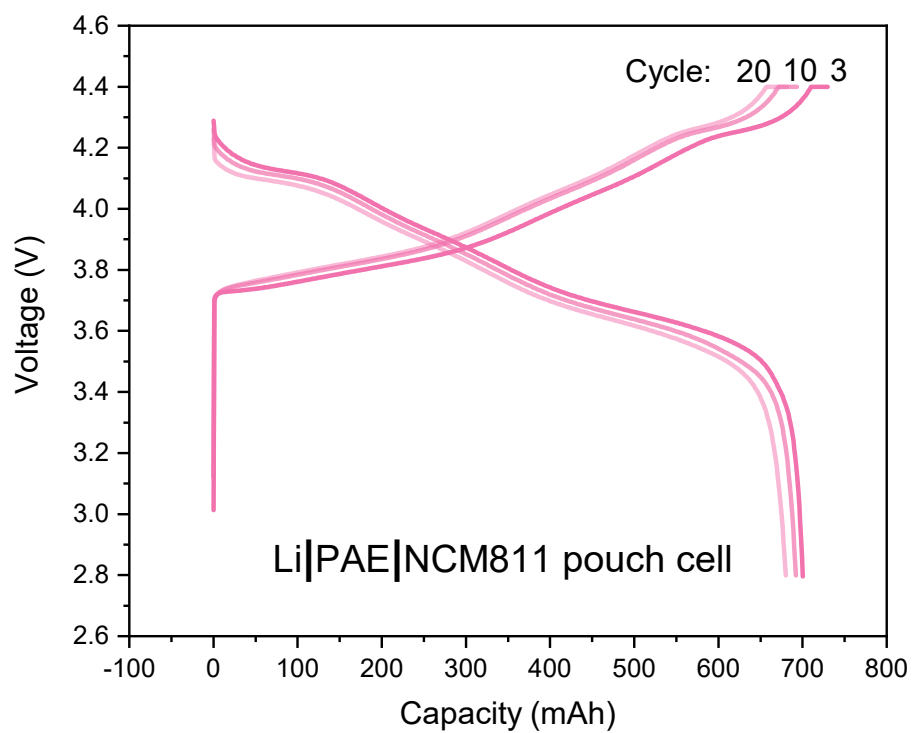


**Fig. S24** Charge–discharge voltage curves of pouch cell using PAE.

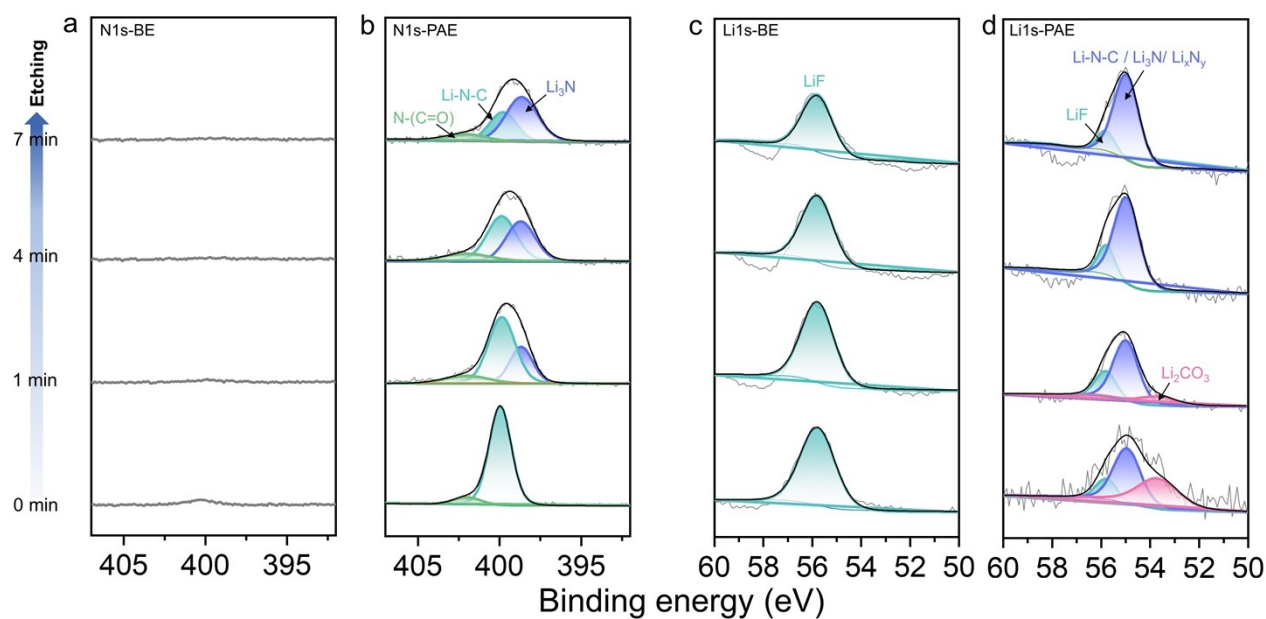


**Fig. S25** N1s HR-XPS data of CEI formed on NCM811 cathode using (a) BE and (b) PAE. Li1s HR-XPS data of CEI formed on NCM811 cathode using c) BE and d) PAE. Etching times include 0, 1, 4, and 7 min. The NCM811 cathode used for TEM and XPS tests was extracted from 50  $\mu\text{m}$  Li||NCM811(4.06 mAh cm<sup>-2</sup>) batteries after 50 cycles.

**Table S1. The ICDD PDF parameters of LiF**

Space group		Fm-3m(225)	
a	4.027 Å	$\alpha$	90.00°
b	4.027 Å	$\beta$	90.00°
c	4.027 Å	$\gamma$	90.00°

**Table S2. The ICDD PDF parameters of Li<sub>2</sub>O**

Space group		Fm-3m(225)	
a	4.611 Å	$\alpha$	90.00°
b	4.611 Å	$\beta$	90.00°
c	4.611 Å	$\gamma$	90.00°



**Table S3. The ICDD PDF parameters of Li<sub>3</sub>N**

Space group		P213(198)	
a	5.500 Å	$\alpha$	90.00°
b	5.500 Å	$\beta$	90.00°
c	5.500 Å	$\gamma$	90.00°

**Table S4. The ICDD PDF parameters of  $\text{Li}_2\text{CO}_3$** 

Space group		I2/a(15)	
a	8.058 Å	$\alpha$	90.00°
b	4.977 Å	$\beta$	109.56°
6.194	6.194 Å	$\gamma$	90.00°

**Table S5. Electrochemical performance comparison of representative polymer electrolytes for LMBs**

Electrolyte formula	Ion transport properties	Cell configuration	N/P ratio	Electrochemical performance [retention/cycles/rate]	Cutting-off Voltage	Ref.
In-situ polymerized polymer electrolytes						
PEGDMA/LiTFSI/PC	0.11 mS cm <sup>-1</sup> at 25 °C	Li  LiFePO <sub>4</sub> (5 mg cm <sup>-2</sup> )	N/A	100%/100/0.1C	3.8 V	(46)
PEGDMA/PETEA/LiPF <sub>6</sub> /EC/DEC/EMC	7.6 mS cm <sup>-1</sup> at RT	Li  LiFePO <sub>4</sub> (3 mg cm <sup>-2</sup> )	N/A	90%/240/0.5C	4.2 V	(47)
1,3-DOL/LiTFSI	1.1 mS cm <sup>-1</sup> at RT	Li  NCM622 (4 mg cm <sup>-2</sup> )	N/A	80%/200/0.5C	4.3 V	(48)
1,3-DOL/LiTFSI	1 mS cm <sup>-1</sup> at RT	Li  LiFePO <sub>4</sub> (5 mg cm <sup>-2</sup> )	N/A	75%/700/1C	4 V	(49)
1,3-DOL/LiTFSI	1.8 mS cm <sup>-1</sup> at RT	Li  NCM622 (3 mg cm <sup>-2</sup> )	N/A	80%/50/0.1C	4.2 V	(50)
1,3-DOL/LiTFSI/DME	3.8 mS cm <sup>-1</sup> at RT	Li  NCM622 (3 mg cm <sup>-2</sup> )	N/A	86%/100/0.5C	4.3 V	(51)
VC/LiTFSI/TEP	4.4 mS cm <sup>-1</sup> at RT	Li  NCM811 (1 mAh cm <sup>-2</sup> )	N/A	87%/200/0.5C	4.3 V	(52)
VC/LiDFOB	0.022 mS cm <sup>-1</sup> at 25 °C	Li  LiCoO <sub>2</sub> (1.5 mg cm <sup>-2</sup> )	N/A	84%/100/0.1C	4.3 V	(53)
PEGDA/LiTFSI/LiBOB/glutaronitrile	1 mS cm <sup>-1</sup> at 30 °C	Li  LiFePO <sub>4</sub> (2-3 mg cm <sup>-2</sup> )	N/A	93%/200/0.2C	3.9 V	(54)
Ex-situ polymer electrolytes						
SN/FEC/LiTFSI/PEA/PEGDAM	1.01 mS cm <sup>-1</sup> at RT	Li  NCM811 (2.3 mAh cm <sup>-2</sup> )	2.3	90%/60/0.2C	4.3 V	(55)
BA/SN/PEGDA/LiTFSI/FEC	1 mS cm <sup>-1</sup> at 20 °C	Li  NCM811 (0.7 mAh cm <sup>-2</sup> )	N/A	80%/25/0.5C	4.3 V	(56)
BA/SN/PEGDA/LiTFSI	1.1 mS cm <sup>-1</sup> at 20 °C	Li  NCM811 (2 mAh cm <sup>-2</sup> )	3.4	88%/100/0.25C	4.3 V	(57)
DOL/MP/LiTFSI/LiPF <sub>6</sub> /FEC	1 mS cm <sup>-1</sup> at -30 °C	Li  NCM811 (1.4 mAh cm <sup>-2</sup> )	N/A	80%/100/0.1C	4.3 V	(58)
PEO/PAN/UFF/LiTFSI	0.068 mS	Li  NCM811	1.1	78%/100/0.	4.3 V	(59)

	$\text{cm}^{-1}$ at 25 °C	(3.6 mAh $\text{cm}^{-2}$ )		1 C		
PVDF-HFP/SiO <sub>2</sub> /ZIF-5/LiPF <sub>6</sub>	1.4 mS $\text{cm}^{-1}$ at RT	Li  NCM811 (1 mAh $\text{cm}^{-2}$ )	>10	90%/300/1 C	4.3 V	(60)
PVDF/LLZTO/PEGMA/FEC/LiTFSI/LiFSI	0.12 mS $\text{cm}^{-1}$ at RT	Li  LiNO <sub>2</sub> (0.8 mAh $\text{cm}^{-2}$ )	4	81%/200/0.5 C	4.4 V	(61)
Diglyme/LiNO <sub>3</sub> /HFiP/LiBOB	1 mS $\text{cm}^{-1}$ at RT	Li  NCM622 (2 mAh $\text{cm}^{-2}$ )	5	80%/200/0.2 C	4.2 V	(62)
PVDF/HFP/LiTFSI/Fluorinated graphene		Li  NCM622 (1.1 mAh $\text{cm}^{-2}$ )	N/A	60%/60/0.2 C	4.3 V	(63)
<b>PAE</b>	<b>1.23 mS <math>\text{cm}^{-1}</math> at 20 °C</b>	<b>Li  NCM811 (4.06 mAh <math>\text{cm}^{-2}</math>)</b>	<b>2.5</b>	<b>&gt;70%/800/0.2C/0.3C</b>	<b>4.4 V</b>	<b>This work</b>

---

**Table S6. The box information for MD simulation of BE**

Number of LiPF <sub>6</sub>	133
Number of EC	1000
Number of DEC	550
Number of FEC	82
Simulation box size (Å <sup>3</sup> )	60 × 60 × 60
Bias temperature (K)	298

**Table S7. The box information for MD simulation of PAE**

Number of LiPF <sub>6</sub>	133
Number of EC	1000
Number of DEC	550
Number of FEC	82
Number of PA monomer	160
Simulation box size (Å <sup>3</sup> )	60 × 60 × 60
Bias temperature (K)	298

## References

- (1) Galvelis, R.; Doerr, S.; Damas, J. M.; Harvey, M. J.; De Fabritiis, G. A scalable molecular force field parameterization method based on density functional theory and quantum-level machine learning. *J. Chem. Inf. Model.* **2019**, *59*, 3485-3493.
- (2) Dodda, L. S.; Cabeza de Vaca, I.; Tirado-Rives, J.; Jorgensen, W. L. LigParGen web server: an automatic OPLS-AA parameter generator for organic ligands. *Nucleic Acids Res.* **2017**, *45*, W331-W336.
- (3) Dodda, L. S.; Vilseck, J. Z.; Tirado-Rives, J.; Jorgensen, W. L. 1.14\* CM1A-LBCC: localized bond-charge corrected CM1A charges for condensed-phase simulations. *J. Phys. Chem. B* **2017**, *121*, 3864-3870.
- (4) Yang, H.; Chen, X.; Yao, N.; Piao, N.; Wang, Z.; He, K.; Cheng, H.-M.; Li, F. Dissolution–precipitation dynamics in ester electrolyte for high-stability lithium metal batteries. *ACS Energy Lett.* **2021**, *6*, 1413-1421.